

# CO band emission from MWC 349

## I. First overtone bands from a disk or from a wind?

**M. Kraus<sup>1</sup>, E. Krügel<sup>1</sup>, C. Thum<sup>2</sup>, and T. Geballe<sup>3</sup>**

<sup>1</sup> Max-Planck-Institut für Radioastronomie, Auf dem Hügel 69, 53121 Bonn, Germany

<sup>2</sup> Institut de Radio Astronomie Millimétrique, F-38406 Saint Martin d'Hères, France

<sup>3</sup> Gemini Observatory, 670 North A'ohoku Place, University Park, Hilo, Hawaii 96720, USA

Received; accepted

**Abstract.** We observed the near infrared emission in the wavelength range 2.28–2.5  $\mu\text{m}$  from the peculiar B[e]-star MWC 349. The spectra contain besides the strong IR continuum the first overtone CO bands and most of the hydrogen recombination lines of the Pfund series, both in emission. We also modeled the spectra. The Pfund lines have a gaussian profile with a FWHM of  $\sim 100$  km/s, and it turned out that their emission is in LTE and optically thin. To explain the CO bands, several scenarios were investigated. We found that the CO band heads are formed under LTE and that the gas must have a temperature of 3500 to 4000 K. The width of the  $2 \rightarrow 0$  band head indicates kinematical broadening of 50 to 60 km/s. We can obtain fits to the measured spectra assuming that the CO gas has a column density of  $5 \cdot 10^{20} \text{ cm}^{-2}$  and is located either at the inner edge of the rotating circumstellar disk. In this case, the disk must have a bulge which partly blocks the radiation so that the observer sees only a sector on the far side where the radial velocities are small. Or the CO emission originates in a wind with gaussian line profiles. Both fits are of equal quality and satisfactory. In a third alternative where the fit is less convincing, the CO emission is optically thin and comes from an extended Keplerian disk.

**Key words:** Line: formation – circumstellar matter – Stars: emission-line, Be – Infrared: stars – Stars: individual: MWC 349

### 1. Introduction

After the discovery of CO band head emission in the BN object by Scoville et al. (1979) a large number of further detections in other young stellar objects (YSO) followed (see e.g. Geballe & Persson 1987; Carr 1989; Chandler et al. 1993; Greene & Lada 1996; Najita et al. 1996).

Several scenarios were discussed to explain the origin of the hot (2500–5000 K) and dense ( $n > 10^{11} \text{ cm}^{-3}$ ) CO component (for some examples see Calvet et al. 1991; Martin 1997),

but the most likely location is a neutral disk or wind (Carr 1989; Chandler, Carlstrom, & Scoville 1995). The disk model is especially supported by high resolution spectroscopic observations of the CO  $2 \rightarrow 0$  band head. The shape of this band head shows for several YSO the kinematic signature of Keplerian rotation (Carr et al. 1993; Carr 1995; Najita et al. 1996) and is a powerful tracer for the existence of a circumstellar disk around young stellar objects.

Also the peculiar B[e]-star MWC 349 shows the first overtone CO bands in emission. These bands were observed first by Geballe & Persson (1987) with a velocity resolution of about 460 km/s.

MWC 349 is a binary system consisting of the main component MWC 349A, classified as a B[e]-star, and the B0 III star companion, MWC 349B, localized  $2''$  west of MWC 349A. We are only interested in the main component, in the following referred to as MWC 349. Its evolutionary state is still unclear. It shows some characteristics of a pre-main sequence B[e]-type star as well as characteristics of a B[e] supergiant (e.g. Lamers et al. 1998).

Cohen et al. (1985) determined its distance (1.2 kpc), bolometric luminosity ( $\sim 3 \cdot 10^4 L_\odot$ ) and the visual extinction towards it ( $A_V^{\text{ISM}} \simeq 10$  mag of which 2 mag might be circumstellar).

The existence of a bulge of circumstellar dust around MWC 349 has been known since long ago (e.g. Geisel 1970). The proposition that MWC 349 also has a disk was supported by observations of double-peaked emission lines (Hamann & Simon 1986, 1988) and by IR speckle interferometry (Leinert 1986; Mariotti et al. 1983) which revealed a disk-like structure of the dust emission in the east-west direction, seen nearly edge on. An accumulation of neutral gas and dust in the equatorial plane of the star is also expected to be responsible for the bipolar structure of the optically thick wind zone seen in the VLA-map of White & Becker (1985). The mass loss rate found for a 50 km/s wind velocity is  $\sim 1.2 \cdot 10^{-5} M_\odot \text{ yr}^{-1}$  (Cohen et al. 1985).

Another indicator for the circumstellar disk are the strong hydrogen recombination maser lines in the mm and submm range which also show the characteristic double-peaked pro-

files (e.g. Martín-Pintado et al. 1989). Recombination lines at different wavelengths sample different regions. With decreasing quantum number  $n$ , i.e. increasing frequency, one sees ionized gas closer to the star. The fact that the rotational velocity of recombination lines with decreasing  $n$  displays a systematical increase led to the assumption that the double-peaked maser emission comes from the ionized atmosphere of a Keplerian rotating disk around a  $25\text{--}30 M_{\odot}$  star (Thum, Martín-Pintado & Bachiller 1992; Thum et al. 1994) whose free-free and free-bound emission was modelled by Kraus et al. (2000). In addition, Rodríguez & Bastian (1994) determined the inclination angle of the disk towards the line of sight to  $15^{\circ} \pm 5^{\circ}$ .

In this paper, we present new low resolution observations of the total first overtone CO band emission as well as high resolution observations of the  $2 \rightarrow 0$  and  $3 \rightarrow 1$  band heads. We discuss the probable location of the hot CO gas by modeling the emission for several scenarios.

## 2. Observations

In 1997 we observed MWC 349 with the UKIRT telescope in the NIR range ( $1.85\text{--}2.5 \mu\text{m}$ ) with a spectral resolution of  $\sim 330 \text{ km/s}$  (Fig. 1a). The spectrum contains several prominent hydrogen and helium recombination lines as well as the first overtone CO bands, all of them in emission.

**Table 1.** Identified lines in the NIR spectrum of MWC 349 (Figs. 1a and b).

number	wavelength [ $\mu\text{m}$ ]	line identification
1	1.86904	He I
2	1.87561	Pa $\alpha$
3	1.89282	C I, Ca I
4	1.90867	He I
5	1.94508	Br $\delta$ , Ca I
6	1.95445	N I
7	1.97470	Si I, C I, N I
8	1.98702	Ca I, C I
9	1.99318	Ca I, Si I, C I
10	2.00130	C I
11	2.05917	He I
12	2.08819	(?) Sn I, Fe II
13	2.11194	He I
14	2.13831	Mg II, C I, Si I
15	2.14359	Mg II, Ca II, [Fe III]
16	2.16611	Br $\gamma$
17	2.20687	Na I doublet, Si I, (?) O II
18	2.21741	C I
19	2.24113	(?) Fe II

In two sessions in 1998 we reobserved MWC 349 in the spectral range  $2.285\text{--}2.341 \mu\text{m}$  with higher spectral resolution ( $10\text{--}15 \text{ km/s}$ ). The observations consist of four separate subspectra with a small overlap at their edges. They are slightly offset relative to each other and at their low wavelength end, the fluxes are systematically overestimated. We calibrated the subspectra by smoothing them to the resolution of the spectrum

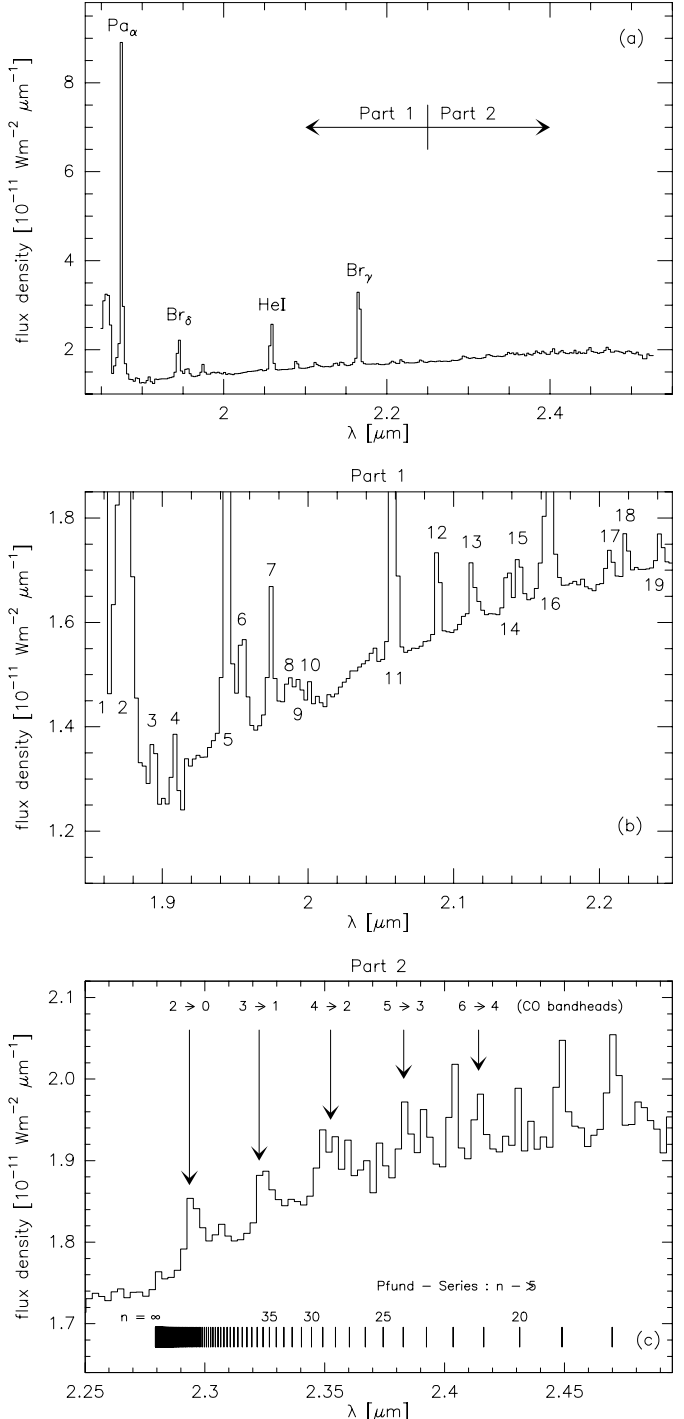


**Fig. 1.** For better visualization, the total NIR spectrum of MWC 349 observed with UKIRT with a spectral resolution of  $\sim 330 \text{ km/s}$  (upper panel) is split in two parts: Part 2 (bottom panel) contains the first overtone CO bands (indicated by the arrows) and most lines from the Pfund series of the hydrogen atom (vertical bars), the remaining spectrum (Part 1, middle panel) contains several emission lines listed in Table 1.

in Fig. 1c, then scaled each spectrum with a factor near  $\sim 1$  and combined them to the final plot of Figure 2.

Unfortunately, the  $3 \rightarrow 1$  band head falls into the overlap region of two subspectra, so its strength is rather uncertain (marked by the dashed line within the figure). This fact turned out during the modeling to be a disadvantage.

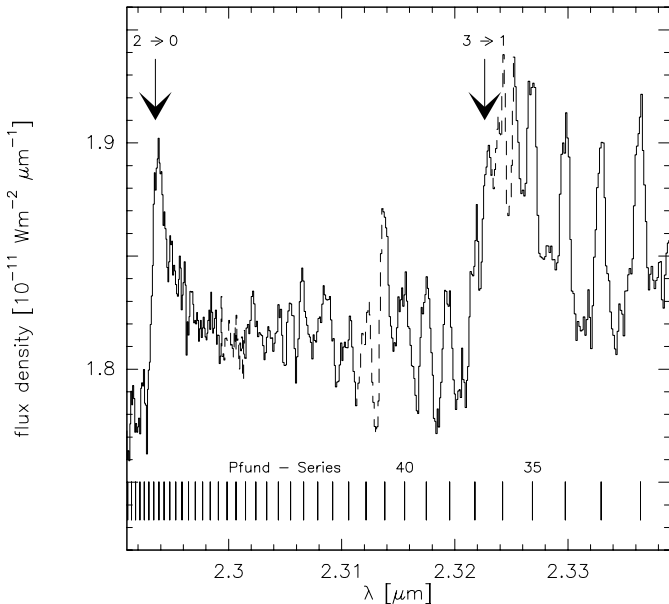


**Fig. 2.** Resulting calibrated high resolution spectrum of the first two CO band heads from MWC 349. The dashed regions mark the overlap for each two subspectra where the calibration is rather uncertain.

### 3. Results

#### 3.1. Hydrogen recombination lines – the Pfund series

As can be seen in Figs. 1c and 2, the spectrum of MWC 349 in the wavelength range from  $2.25$  to  $2.5 \mu\text{m}$  contains beside the first overtone CO bands also the Pfund series (transitions of the form  $n \rightarrow n' = 5$ , denoted as  $\text{Pf}(n)$ ) of the hydrogen atom. Hamann & Simon (1986) already identified some of them in their velocity-resolved infrared spectroscopy of MWC 349, but their resolution of  $\sim 20 \text{ km/s}$  was lower than ours, so they could only resolve lines up to  $\text{Pf}(34)$ . Their FWHM values of several unsmeared lines were about  $100 \text{ km/s}$  and agree with ours.

Many of the other emission lines they observed are double-peaked which is a hint for a rotating medium. At first glance we cannot exclude the Pfund lines to take part of the rotation because they are superimposed on the CO bands, but their profile looks more than a gaussian than a double-peaked one. A gaussian velocity component of about  $50 \text{ km/s}$ , however, is not a surprising feature for MWC 349. Also the cm and mid IR hydrogen recombination lines as well as the 'pedestal' feature of the double-peaked mm recombination maser lines show such a velocity component (Smith et al. 1997; Thum, Martín-Pintado & Bachiller 1992). It is often ascribed to the wind of MWC 349.

To model the hydrogen emission, we assume the Pfund lines to be optically thin. Their intensity is given by

$$I_\nu = N_n A_{n,5} h \nu \Phi_H(\nu). \quad (1)$$

To evaluate it, we need the number density  $N_n$  of the atoms in level  $n$ , the Einstein coefficients,  $A_{n,5}$ , and the profile function of the hydrogen gas,  $\Phi_H(\nu)$ .

In view of the measured line widths, we choose a gaussian profile function defined as

$$\Phi_H(\nu) = \frac{1}{\sqrt{\pi} \frac{\nu_0}{c} v} \exp \left[ - \left( \frac{\nu - \nu_0}{\frac{\nu_0}{c} v} \right)^2 \right] \quad (2)$$

$v$  is the most probable velocity which is in the case of the thermal velocity given by  $v = \sqrt{2kT/m}$  for particles having a Maxwellian velocity distribution. In our case,  $v \simeq 50 \text{ km/s}$ . We also take into account the local standard of rest velocity of  $\sim 8 \text{ km/s}$  (Thum, Martín-Pintado & Bachiller 1992; Thum et al. 1995).

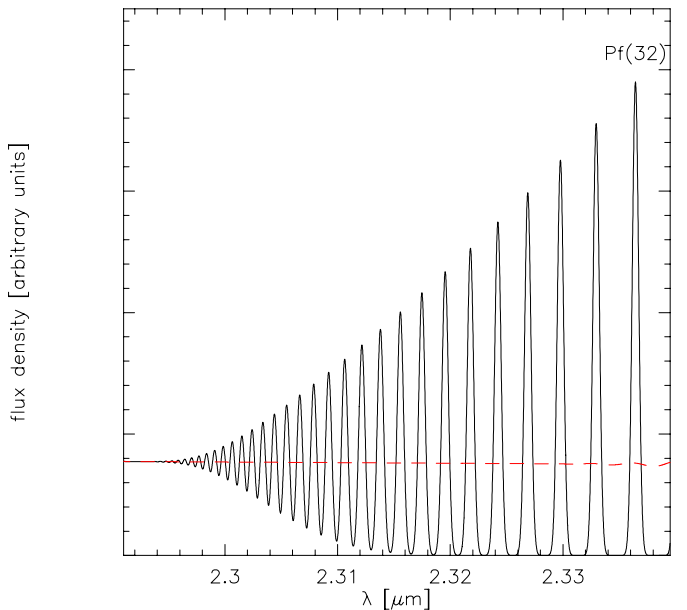


**Fig. 3.** Spectrum of optically thin Pfund lines in LTE, with an isothermal electron temperature of  $T_e = 10^4 \text{ K}$  and a gaussian velocity component of  $50 \text{ km/s}$ . The spectral resolution to which the lines were smoothed are  $330 \text{ km/s}$  (dashed line) and  $15 \text{ km/s}$  (solid line). At short wavelengths, the lines blend into a 'continuum', especially for the low resolution.

The Einstein coefficients,  $A_{nn'}$ , can be calculated, following Menzel & Pekeris (1935). If we restrict ourselves to Pfund lines with  $n \geq 18$  (see Fig. 1c), they can be approximated by

$$A_{n,5} \simeq 3.023 \cdot 10^9 n^{-5.005}. \quad (3)$$

The number density,  $N_n$ , of the level  $n$  follows from Saha's equation

$$N_n = b_n N_i N_e g_n \frac{h^3}{2 (2\pi m_e k T_e)^{3/2}} e^{\frac{h R_y}{n^2 k T_e}} \quad (4)$$

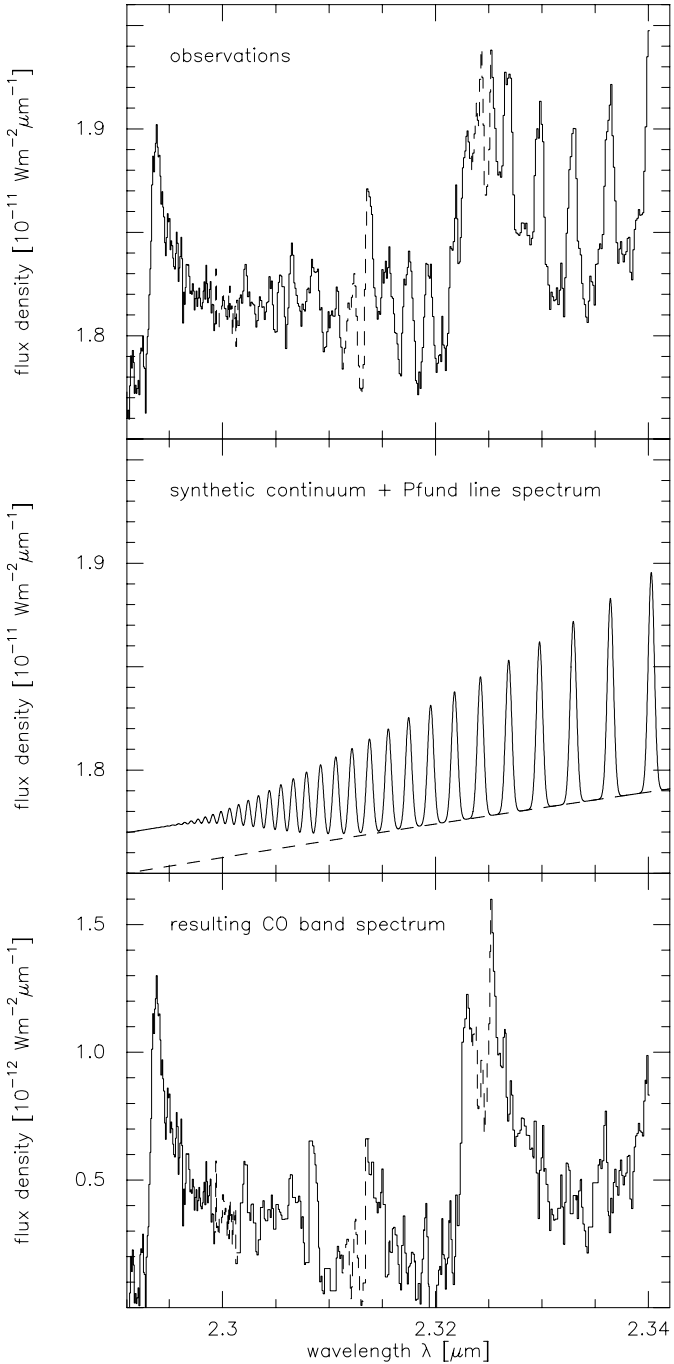


**Fig. 4.** Subtraction of the synthetic continuum and Pfund line emission (solid line, middle panel, pure continuum is shown by the dashed line) from the observations (upper panel) leads to the almost pure CO first overtone band emission (lower panel).

where  $N_i$  and  $N_e$  are the number densities of the protons and electrons,  $T_e$  and  $m_e$  are the electron temperature and electron mass,  $g_n = 2n^2$  is the statistical weight of the state  $n$ , and  $Ry$  is the Rydberg constant. The  $b_n$ -factors which describe the deviation from LTE and which depend on the electron temperature and density were taken from the electronic Tables of Storey & Hummer (1995) for Menzel's case B recombination theory.

Detailed modeling of the Pfund line spectrum performed by Kraus (2000) showed that the emission arises within the innermost parts of the ionized wind where the electron densities are highest. Within these regions it is expected that  $N_e \leq 10^9 \text{ cm}^{-3}$ . Electron densities as high as  $10^8 \text{ cm}^{-3}$  have already been found by Streltitski et al. (1996) and Thum et al. (1998). For such high electron densities the emission is clearly in LTE, i.e. the  $b_n$ -factors are  $\sim 1$ . Therefore, non LTE effects are negligible.

In our case of optically thin Pfund lines in LTE and with a constant electron temperature the intensity ratios of two neighbouring Pfund lines is according to Eq. (1) independent of the electron density

$$\frac{I_{\text{Pf}(n+1)}}{I_{\text{Pf}(n)}} \sim \left( \frac{n}{n+1} \right)^{5.005} \cdot \exp \left( -\frac{hRy}{kT_e} \frac{2n+1}{(n^2+n)^2} \right). \quad (5)$$

and always smaller than 1, which means that the intensity of the Pfund lines decreases with increasing quantum number. This behaviour can qualitatively be seen in Fig. 3 where we plotted the synthetic Pfund lines which we smoothed to the spectral resolution of 10–15 km/s (solid line) and 330 km/s (dashed line), respectively. The wavelength difference between the neighbouring Pfund lines decreases with increasing  $n$  leading to a blend of the individual lines. The onset of this blend depends on the width of the lines and on the spectral resolution and leads to a hydrogen 'continuum'.

**Table 2.** Parameters for hydrogen used for the calculations of the Pfund lines shown in Fig. 4 (middle panel).

$T_e$ [K]	$v_{\text{gauss}}$ [km/s]	$A_v^{\text{ISM}}$ [mag]	$\int N_e^2 dV$ [cm $^{-3}$ ]
$\leq 10^4$	$\sim 50$	10	$6.35 \cdot 10^{60}$

The interstellar visual extinction towards MWC 349 is about  $A_v^{\text{ISM}} \simeq 10$  mag and has to be taken into account. Fitting the Pfund lines with the parameters displayed in Table 2 leads to the quantity  $\int N_e^2 dV$ , where  $V$  is the volume of the emitting region.

The middle panel of Figure 4 contains the modelled Pfund series added to the continuum emission of MWC 349 (dashed line) taken from Kraus et al. (2000). These two components were subtracted from the observations (upper panel) and the resulting spectrum (lower panel) can mainly be ascribed to the CO first overtone band emission. To fit this observed CO spectrum is the aim of the following sections.

### 3.2. Theory of the CO bands

The energy of a diatomic molecule in rotational level  $J$  and vibrational level  $v$  can be expanded in the following way (Dunham 1932a, 1932b)

$$E(v, J) = hc \sum_{k,l} Y_{k,l} \left( v + \frac{1}{2} \right)^k (J^2 + J)^l. \quad (6)$$

The parameters  $Y_{k,l}$  are for the CO molecule taken from Farrenq et al. (1991). The first overtone bands result from coupled vib-rot transitions in the ground electronic state and obey the selection rules  $\Delta v = 2$  and  $\Delta J = \pm 1$ .

In the following, we assume the CO gas to be in LTE. Then, the levels are populated following a Boltzmann distribution,

$$N_{vJ} = \frac{N}{Z} (2J+1) e^{\frac{-E(v,J)}{kT}} \quad (7)$$

where  $N$  and  $T$  are the total number density and temperature of CO molecules and  $Z$  is the total partition function, given as the product of the vibrational and the rotational partition function

$$Z = Z_v \cdot Z_J = \sum_v e^{\frac{-E_v}{kT}} \cdot \sum_J (2J+1) e^{\frac{-E_J}{kT}}. \quad (8)$$

To account for optical depth effects, we calculate the line intensities from the transfer equation

$$I_\nu = B_\nu(T) (1 - e^{-\tau_\nu}). \quad (9)$$

The optical depth is  $\tau_\nu = \int \kappa_\nu ds$  with the absorption coefficient per cm

$$\kappa_\nu = \frac{c^2 N_{vJ} A_{vJ;v'J'}}{8\pi\nu^2} \left( \frac{2j+1}{2j'+1} \cdot \frac{N_{v'J'}}{N_{vJ}} - 1 \right) \Phi_{\text{CO}}(\nu) \quad (10)$$

where  $\Phi_{\text{CO}}(\nu)$  is the profile function of the CO gas. The Einstein coefficients,  $A_{vJ;v'J'}$ , are from Chandra, Maheshwari & Sharma (1996).

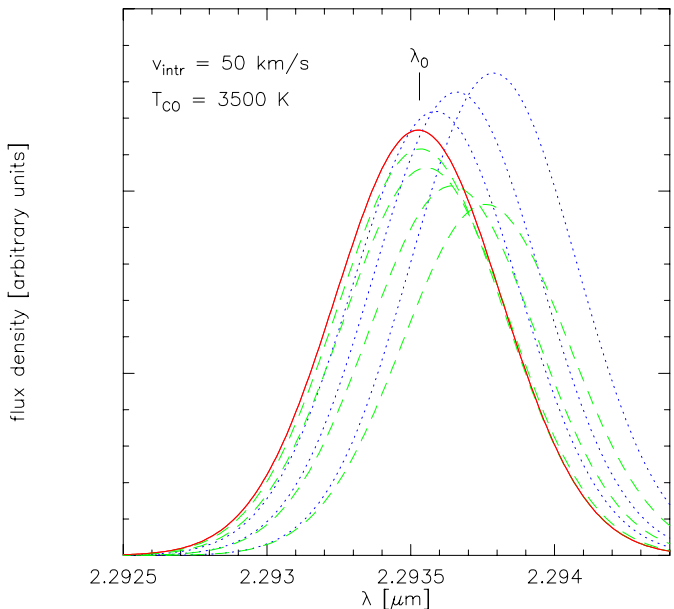


**Fig. 5.** Individual vib-rot lines that form the  $2 \rightarrow 0$  band head. The solid curve is the  $(2, 51) \rightarrow (0, 50)$  transition. The dotted curves are the neighbouring transitions with rotational quantum numbers decreasing in steps of one; for the dashed curves, the quantum numbers increase in steps of one.

Let  $\lambda_{\text{min}}$  denote the onset of the  $(2 \rightarrow 0)$  bandhead. We define it to be the wavelength where the intensity of the  $(2, 51) \rightarrow$

$(0, 50)$  line (see Fig. 5) has dropped by a factor  $x \sim 5$  from its maximum at  $\lambda_0$ ; the exact number is not important. We determine  $\lambda_{\text{min}}$  from Figure 6 to  $(2.29285 \pm 0.00005) \mu\text{m}$ .

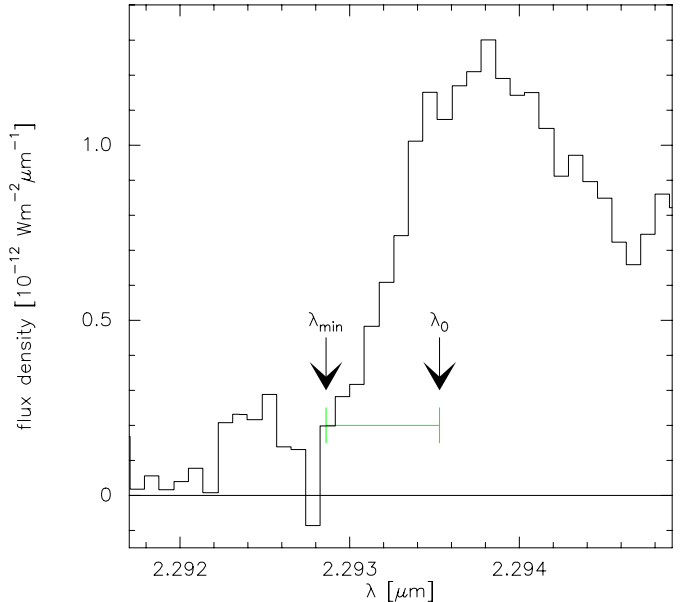


**Fig. 6.** The onset of the spectrum above noise is chosen as the minimum wavelength  $\lambda_{\text{min}}$ .

The value of  $\lambda_{\text{min}}$  depends of course on the various mechanisms of line broadening. Most processes lead to a gaussian or nearly gaussian profile, like thermal (turbulent) motion of mean velocity  $v_{\text{th}}$  ( $v_{\text{turb}}$ ), detector resolution  $v_{\text{res}}$ , spherical wind  $v_{\text{wind}}$  (see e.g. Hamann & Simon 1986). Their superposition results again in a gaussian line of width  $v_{\text{gauss}} = \sqrt{v_{\text{th}}^2 + v_{\text{turb}}^2 + v_{\text{wind}}^2 + v_{\text{res}}^2}$ .

Disk rotation, on the other hand, produces a double-peaked profile. In a gas ring rotating at velocity  $v_{\text{rot}}$  a line with laboratory frequency  $\nu_0$  is shifted up to a maximum frequency  $\nu_0 \cdot (1 + v_{\text{rot}}/c)$ . In a mixture of disk rotation and gaussian broadening one finds the following expression for the minimum wavelength,

$$\frac{1}{\lambda_{\text{min}}} = \frac{1}{\lambda_0} \left[ 1 + \frac{v_{\text{lsr}} + v_{\text{rot}}}{c} \right] \left[ \frac{v_{\text{gauss}}}{c} \sqrt{\ln x} + 1 \right], \quad (11)$$

where  $v_{\text{lsr}} = 8 \text{ km/s}$  is the velocity shift of MWC 349 with respect to the local standard of rest. This relation only holds if the emission in the rise of the spectrum is optically thin. The thermal velocity  $v_{\text{th}}$  of CO molecules at 3500 K is less than  $\sim 1 \text{ km/s}$  and negligible in comparison with the spectral resolution  $v_{\text{res}} = 10 \dots 15 \text{ km/s}$ . The same can be said about the turbulent velocity which is not likely to exceed the speed of sound.

Eq. (11) can now be used to relate  $v_{\text{wind}}$  to the rotational velocity  $v_{\text{rot}}$ . The result is shown in Figure 7. The dashed lines above and below the solid line are for the lower and upper limit of  $\lambda_{\text{min}}$ . If the CO gas performs no rotation, the gas must emanate from the disk in a wind with about  $\sim 50 \text{ km/s}$ , the same

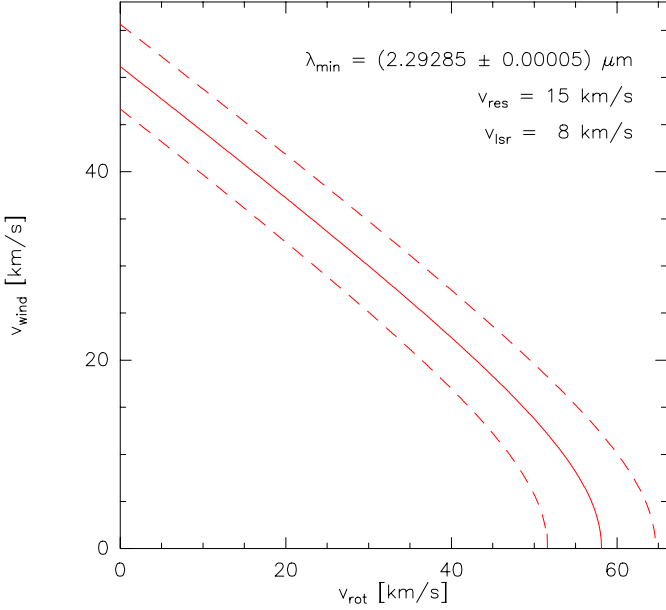


**Fig. 7.** The dependence of  $v_{\text{wind}}$  on  $v_{\text{rot}}$  after Eq. (11) is shown.  $x = 10$ , and the remaining parameters are chosen as indicated in the Figure. The solid line is for  $\lambda_{\text{min}} = 2.29285 \mu\text{m}$ , the dashed line above (below) is for the lower (upper) limit of  $\lambda_{\text{min}}$ .

velocity as for the Pfund lines. Without a wind, one derives a rotational velocity of  $\sim 58 \pm 7 \text{ km/s}$ . This value is larger than other rotational velocities around MWC 349 observed up to now, the highest being 42.5 km/s for He I (Hamann & Simon 1986).

#### 4. Modeling the CO band emission

##### 4.1. A gaussian line profile for the CO gas

First, we neglect rotation and assume a pure gaussian line profile. The velocity of the CO gas is taken from Figure 7 as  $v_{\text{gauss}} \approx 50 \text{ km/s}$ .

For the calculation of the optical depth we assume the absorption coefficient to be constant along the line of sight. Then  $\tau_{\nu}$  is simply given as the product of the absorption coefficient per CO molecule,  $\kappa_{\nu}$ , times the CO column density,  $\tau_{\nu} = \kappa_{\nu} \cdot N_{\text{CO}}$ .

In Fig. 8 we plotted  $\kappa_{\nu}$  for temperatures between 3000 K and 5000 K, and a gaussian velocity of the gas of 50 km/s. In the wavelength range around the  $3 \rightarrow 1$  band head ( $2.322\text{--}2.325 \mu\text{m}$ ) the absorption coefficient is higher than in the region around the  $2 \rightarrow 0$  band head ( $2.293\text{--}2.295 \mu\text{m}$ ). This effect becomes stronger with increasing temperature. Thus, the turnover from optically thin to optically thick emission depends not only on the column density but also on the temperature: the  $3 \rightarrow 1$  band head becomes optically thick at lower temperature and lower column density than the  $2 \rightarrow 0$  band head.

Next, we vary the CO column density and fix  $T_{\text{CO}}$  at 4000 K. The synthetic spectra in Figure 9 are calculated for the case of extreme optical depth (upper line) and for CO column

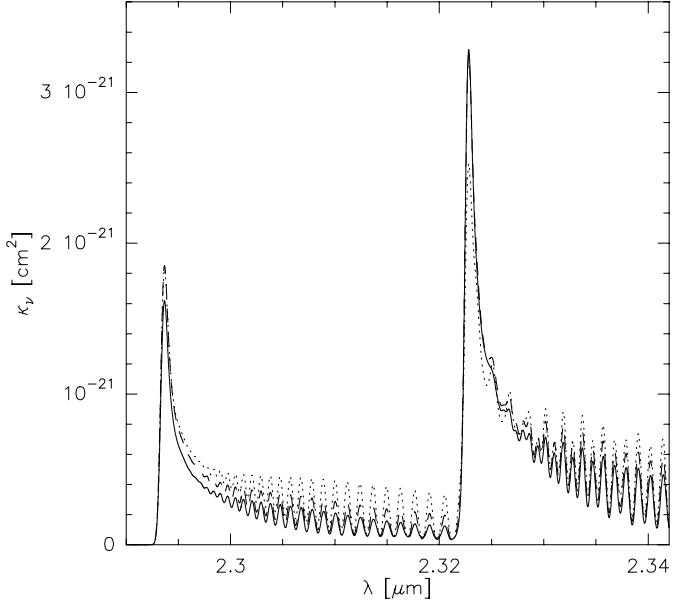


**Fig. 8.** Absorption coefficient per CO molecule,  $\kappa_{\nu}$ , for temperatures of 3000 K (dotted line), 4000 K (dashed line), and 5000 K (solid line). The gaussian velocity of the CO gas is 50 km/s.

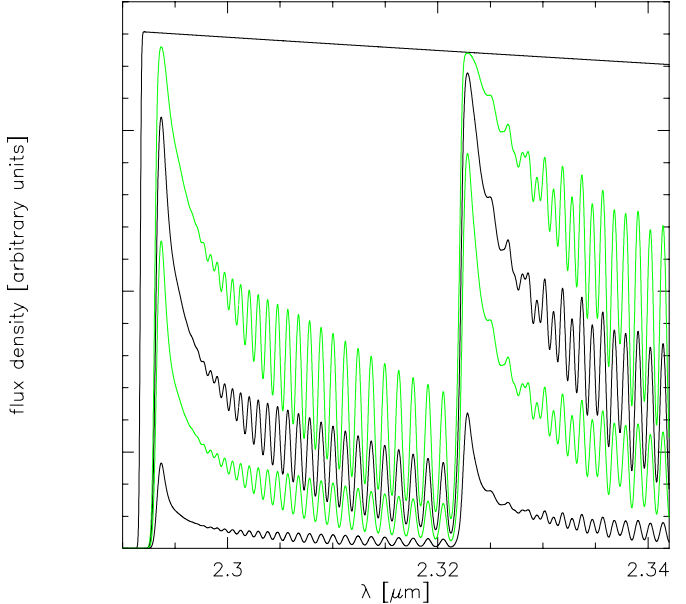


**Fig. 9.** Calculated CO band emission spectra for a temperature of the CO gas of 4000 K, a gaussian velocity of  $\sim 50 \text{ km/s}$ , and a CO column density increasing from bottom to top:  $10^{20}$ ,  $5 \cdot 10^{20}$ ,  $10^{21}$ , and  $2 \cdot 10^{21} \text{ cm}^{-2}$ . The upper line represents the case for  $\tau \rightarrow \infty$ .

densities (from top to bottom) of  $2 \cdot 10^{21}$ ,  $10^{21}$ ,  $5 \cdot 10^{20}$ , and  $10^{20} \text{ cm}^{-2}$ . With increasing column density the optical depth enlarges and the intensity tends towards its limiting blackbody value. In addition, the spectra show two characteristic features: a varying intensity ratio of the two band heads and a broadening of the band head structure.

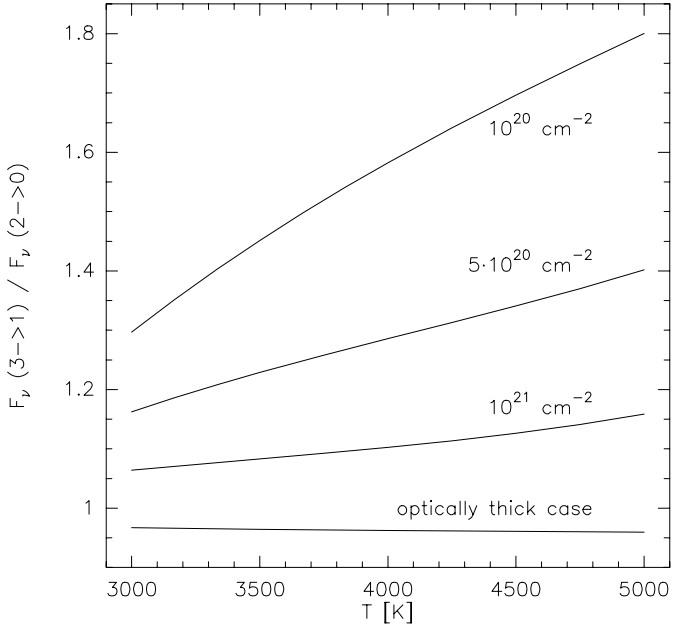


**Fig. 10.** The flux density ratio of the  $3 \rightarrow 1$  and  $2 \rightarrow 0$  band heads as a function of temperature and column density. The ratio is highest in the optically thin case ( $N_{\text{CO}} \leq 10^{20} \text{ cm}^{-2}$ ) and approaches  $\simeq 0.96$  for  $\tau \rightarrow \infty$ .

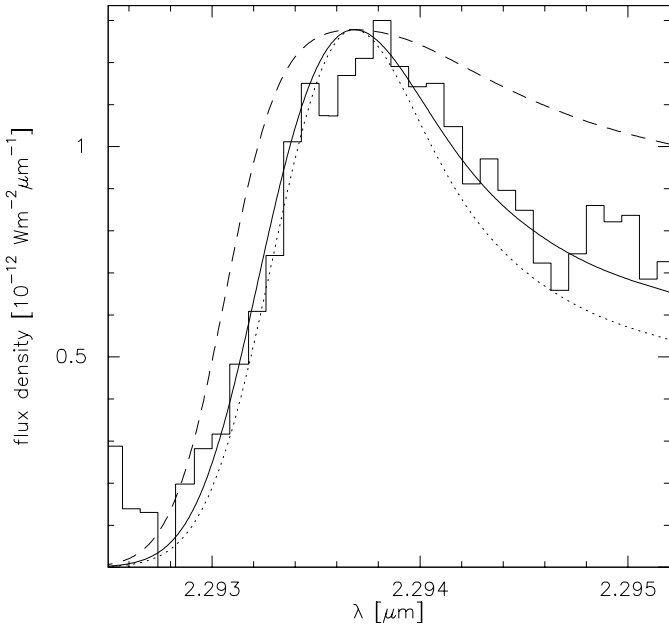


**Fig. 11.** Theoretical ( $2 \rightarrow 0$ ) CO band head emission for a gaussian line profile with  $v_{\text{gauss}} \sim 50 \text{ km/s}$ . The CO column density is  $2 \cdot 10^{21} \text{ cm}^{-2}$  (dashed line),  $5 \cdot 10^{20} \text{ cm}^{-2}$  (solid line), and  $10^{20} \text{ cm}^{-2}$  (dotted line).

The first property can better be seen in Figure 10 where we plotted the flux density ratio of the  $3 \rightarrow 1$  and  $2 \rightarrow 0$  band head with temperature for different column densities. This ratio decreases with increasing column density, i.e. increasing  $\tau$ , and approaches 0.96 for  $\tau \rightarrow \infty$ .

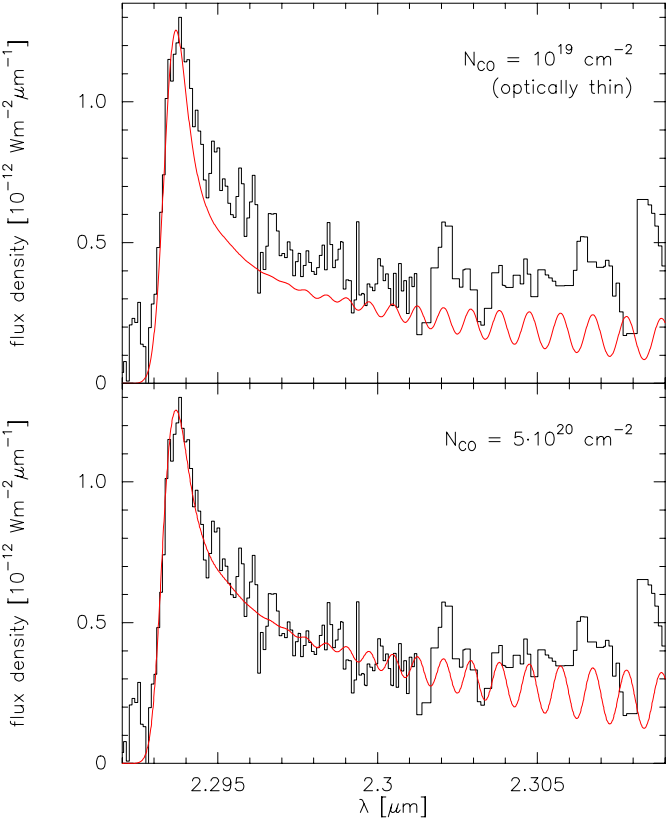


**Fig. 12.** Comparison between theoretical ( $2 \rightarrow 0$ ) band head spectra of optically thin (upper panel) and marginally optically thick emission (lower panel). In both cases, the temperature is 3500 K.

The determination of the column density with only the help of this ratio is, however, not definite because the flux density ratio also depends on temperature. From our observations we get no information at all on the column density in this way because the observed strength of the  $3 \rightarrow 1$  band head is subject to some uncertainty as discussed in Section 2.

The second characteristic feature is the broadening of the band head structure with increasing column density, especially at the long wavelength side. In Figure 11 the observed  $2 \rightarrow 0$  band head region (histogram) is overlaid on the theoretical spectra with column densities of  $2 \cdot 10^{21} \text{ cm}^{-2}$  (dashed line),  $5 \cdot 10^{20} \text{ cm}^{-2}$  (solid line), and  $10^{20} \text{ cm}^{-2}$  (optically thin case, dotted line).

At first glance, it seems that the observations might also be fitted by optically thin emission, but the upper panel of Figure 12 which includes a somewhat larger wavelength interval is clearly inconsistent with the optically thin case whereas the observations can be reconciled with a synthetic spectrum of column density  $N_{\text{CO}} \simeq 5 \cdot 10^{20} \text{ cm}^{-2}$  (lower panel of Figure 12). An additional disagreement is that the flux density ratio of the bandheads is highest for the optical thin case which can not be confirmed by the observations.

So we take  $N_{\text{CO}} = 5 \cdot 10^{20} \text{ cm}^{-2}$  as the best fit CO column density. The synthetic spectra of the  $2 \rightarrow 0$  band head look very similar for temperatures in the range of  $3000 - 5000 \text{ K}$ . For a

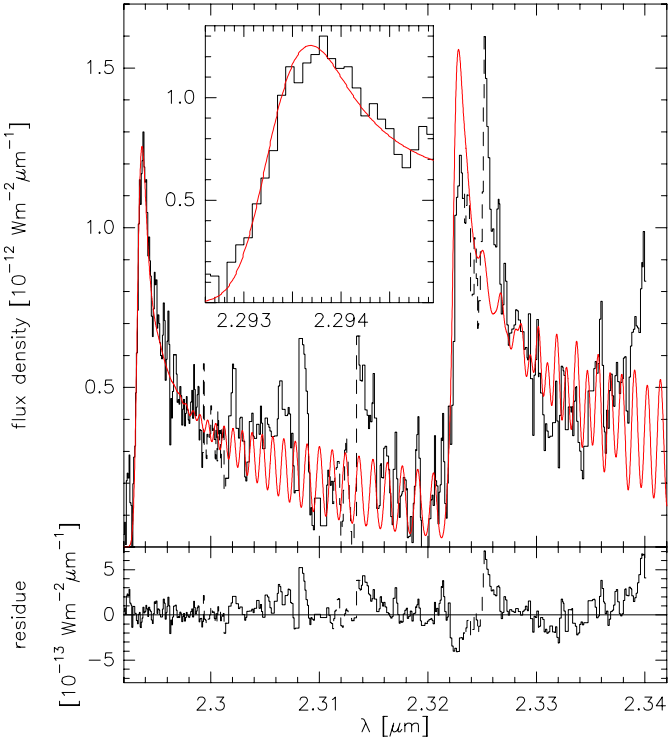


**Fig. 13.** Modelled CO band emission (black line) for a temperature of  $T_{\text{CO}} = 3500$  K and a gaussian velocity of  $\sim 50$  km/s overlaid on the observations (grey histogram). The model parameters are given in Table 3. The insert shows a blow-up of the  $2 \rightarrow 0$  band head. Lower panel: residue of observations minus model. Some yet unidentified emission lines seem to be present.

more sensitive limitation of the temperature range we must take a look at the  $3 \rightarrow 1$  band head. From there we conclude that  $T_{\text{CO}} = 3500\text{--}4000$  K. Unfortunately, an exact determination of the CO temperature fails because the higher bandheads are not available within our high resolution spectrum.

**Table 3.** Parameters for CO used for the calculations shown in Fig. 13.  $A_{\text{v}}^{\text{ISM}}$  denotes the foreground extinction,  $A_{\text{CO}}$  and  $M_{\text{CO}}$  are the emitting CO area projected to the sky and the mass of CO derived from the fit, respectively.

$N_{\text{CO}}$ [cm $^{-2}$ ]	$T_{\text{CO}}$ [K]	$v_{\text{gauss}}$ [km/s]	$A_{\text{v}}^{\text{ISM}}$ [mag]	$A_{\text{CO}}$ [cm $^2$ ]	$M_{\text{CO}}$ [g]
$5 \cdot 10^{20}$	3500	$\sim 50$	10	$1.36 \cdot 10^{26}$	$3.2 \cdot 10^{24}$

With the derived values for column density and temperature we model the synthetic CO band spectrum taking into account the foreground extinction,  $A_{\text{v}}^{\text{ISM}}$ , and fitted it to the observations (Figure 13; Table 3 summarizes the parameters used). The lower panel of Fig. 13 shows the residue of observed minus calculated spectrum. Some remaining features may result from observational uncertainties (indicated as dashed parts), for example the dip around  $2.3225\text{ μm}$  and the region around

$2.314\text{ μm}$ , whereas the features at  $2.3253$  and  $2.3084\text{ μm}$  seem to be yet unidentified emission lines.

For a distance to MWC 349 of 1.2 kpc we find a CO emission area projected on the sky of  $A_{\text{CO}} \simeq 1.36 \cdot 10^{26}\text{ cm}^2$  and a mass of  $M_{\text{CO}} \simeq 3.2 \cdot 10^{24}\text{ g}$ . Our  $A_{\text{CO}}$  is about 5 times larger than the value of  $2.5 \cdot 10^{25}\text{ cm}^2$  found by Geballe & Persson (1987) who could only derive a lower limit.

#### 4.2. CO bands from a Keplerian rotating disk

We investigate whether the CO bands in MWC 349 can alternatively be explained by emission from the circumstellar disk. For demonstration, we first calculate the optically thin emission from an infinitesimally narrow ring. For Kepler rotation, the orbital velocity is

$$v_{\text{rot}} = \sqrt{GM_{*}/r}. \quad (12)$$

and the line of sight velocity,  $v_{\text{los}}$ , of a gas element in the ring

$$v_{\text{los}} = v_{\text{rot}} \cdot \cos \theta \cdot \cos i. \quad (13)$$

Here  $G$  denotes the gravitational constant,  $r$  the ring radius,  $M_{*}$  the stellar mass,  $i$  the inclination angle of the ring, and  $\theta$  the azimuthal angle. The resulting profile of the CO band head smoothed to the observational resolution of 15 km/s shows a characteristic shoulder at short and a maximum at long wavelengths relative to an unbroadened band head (see Fig. 14). The distance between shoulder and maximum decreases with decreasing orbital velocity. The CO profile of a rotating ring is evidently very different from what is observed in MWC 349.

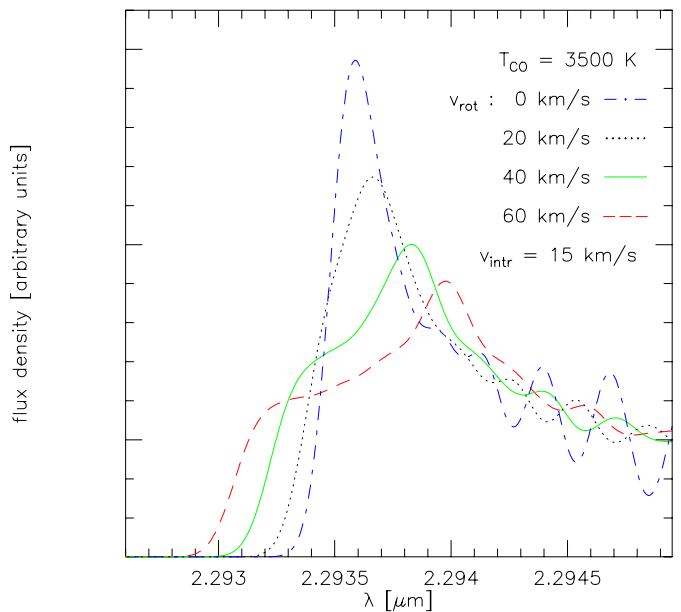


**Fig. 14.** Optically thin CO band emission from rings of constant rotational velocity ( $v_{\text{rot}} = 60, 40, 20$  and  $0$  km/s) and for an inclination angle of  $i = 0^\circ$ . The spectra are smoothed to the observational resolution of 15 km/s.

We next calculate the emission from a whole disk viewed nearly edge-on, using the radiative transfer of Eq. (9). We assume power laws for the temperature and surface density,

$$T(r) = T_0 \cdot \left( \frac{r}{r_i} \right)^{-p} = T_0 \cdot \left( \frac{v}{v_i} \right)^{2p} \quad (14)$$

and

$$\Sigma(r) = \Sigma_0 \cdot \left( \frac{r}{r_i} \right)^{-q} = \Sigma_0 \cdot \left( \frac{v}{v_i} \right)^{2q}. \quad (15)$$

$r_i$  is the inner radius of the Kepler disk where the rotational velocity has its maximum value  $v_i$ . We fix the inner radius by putting  $v_i = 60$  km/s (see Figure 7). Further, we assume  $T_0 = 5000$  K, which is the dissociation limit of CO molecules, and an inclination angle of  $10^\circ$ . The radius  $r_{\text{out}}$ , out to which the CO (2→1) band is thermally excited, is a free parameter; the velocity there equals  $v_{\text{out}}$ . For these disk calculations we surmise that the CO bands at 2 micron are for radii greater than  $r_{\text{out}}$  only subthermally excited due to lower densities. Therefore their contribution to the overall spectrum is probably small. The CO disk is geometrically flat so that along each line of sight through the inclined disk the density and temperature are constant. The total flux from the disk is obtained from a straight forward numerical integration.

**Table 4.** Parameters for the fit of the CO disk calculations shown in Fig. 15. Fixed parameters are the mass of  $26 M_\odot$ ,  $T_0 = 5000$  K,  $p = 0.5$ ,  $q = 1.5$ , and  $v_i = 60$  km/s which leads to  $r_i \simeq 6.4$  AU.

$v_{\text{out}}$ [km/s]	$r_{\text{out}}$ [AU]	$T(r_{\text{out}})$ [K]	$N_0$ [cm $^{-2}$ ]	$N(r_{\text{out}})$ [cm $^{-2}$ ]
40	14.4	3333	$8.5 \cdot 10^{16}$	$2.5 \cdot 10^{16}$
30	25.6	2500	$5.8 \cdot 10^{16}$	$7.3 \cdot 10^{15}$

By a systematic variation of the free parameters ( $\Sigma_0, v_{\text{out}}, p, q$ ), we find that the shape of the spectrum is strongly influenced by the column density at the inner edge and by the size of the disk, whereas the exponents  $p$  and  $q$  play a minor role; we therefore fix them following Hayashi (1981) to  $p = 0.5$  and  $q = 1.5$ . Similar numbers are derived for the dust disk (Kraus et al. 2000).

The disk models then contain only two free parameters: the outer radius,  $r_{\text{out}}$ , and the column density at the inner edge,  $N_0$ . To explain the observed band head profile with a rotating disk, one needs a large spread in the rotational velocity because otherwise one cannot suppress the shoulders seen in Fig. 14. The large velocity spread implies a large emitting area, and therefore a low column density, so that the emission becomes very optically thin ( $\tau \simeq 10^{-4}$ ), even at the inner edge of the CO disk. The outer velocity  $v_{\text{out}}$  must lie in the range between 30 and 40 km/s. If  $v_{\text{out}}$  were higher, the shoulder of the band head would become too broad, if it were smaller, the profile would get too narrow. Our best models of a rotating disk are

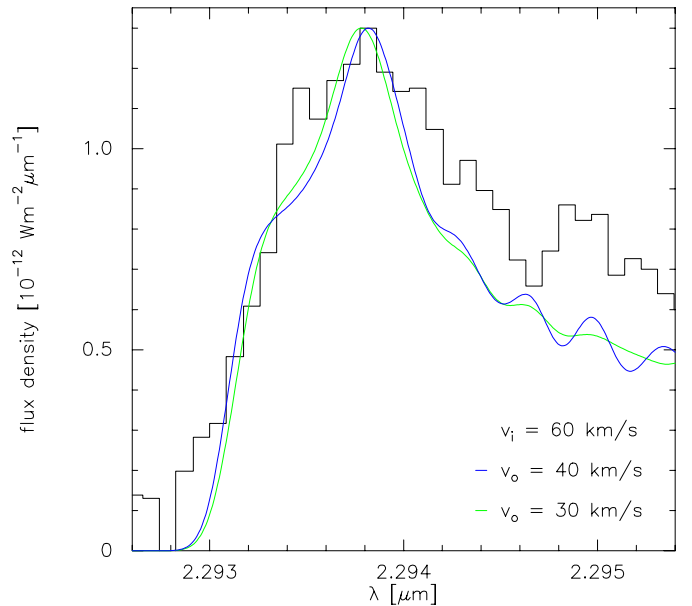


**Fig. 15.** Best fit to the observations (histogram) by Kepler disk. Model parameters from Table 4.

presented in Fig. 15. Considering the quality of the data, they are marginally acceptable.

We add that if one assumes dust and gas to be thermally decoupled, it is in these models nevertheless possible that the strength of the CO band head amounts to  $f \sim 5\%$  of the continuum, as observed, although the CO emission is very optically thin. As the dust emits like a blackbody, the equation  $f B_\nu(T_d) = \tau_\nu B_\nu(T_{\text{CO}})$  is approximately fulfilled for  $T_d \sim 1000$  K,  $T_{\text{CO}} \sim 4000$  K and  $\tau \sim 10^{-4}$ .

## 5. Discussion

Mathematically, there is also the possibility to combine the wind model of Fig. 11 (solid line), which is based on a gaussian profile of  $\sim 50$  km/s half width, with a Kepler rotation as long as  $v_{\text{rot}} \leq 40$  km/s. This is shown in Figure 16, where a rotational component with  $v_{\text{rot}} = 40$  km/s (black curve) is added to the gaussian velocity profile. Otherwise the basic parameters are the same as for the wind (LTE; CO column density  $\sim 5 \cdot 10^{20}$  cm $^{-2}$ ;  $T_{\text{CO}} = 3500 \dots 4000$  K).

Although the fit is again very good, this scenario meets the following difficulties: If the rotational velocity  $v_{\text{rot}} \leq 40$  km/s, the stellar mass of  $26 M_\odot$  implies a distance greater than 14 AU. If the CO gas is coupled to the dust, it should have the same temperature of  $\sim 950$  K as the dust grains at that distance (Kraus et al. 2000), which is much too low. If CO is located above the disk and thermally decoupled from the dust, it might achieve the required temperature of  $\sim 3500$  K by radiative heating. But the CO column density of  $5 \cdot 10^{20}$  cm $^{-2}$  then implies a gas surface density which is at least an order of magnitude greater than what follows from the dust disk (adopting standard conversion factors  $\Sigma_{\text{dust}} : \Sigma_{\text{H}} \simeq 10^{-2}$ ,  $N_{\text{CO}} : N_{\text{H}} \simeq 10^{-4}$ ).

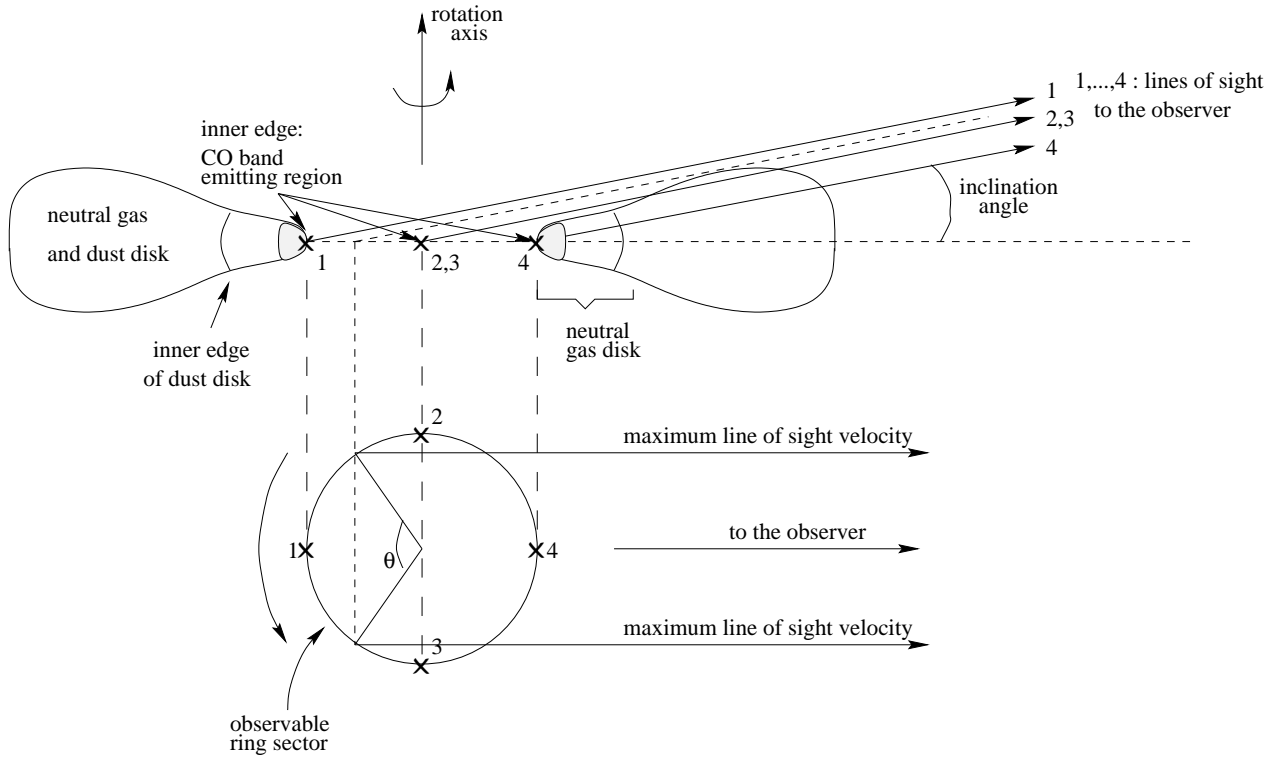


**Fig. 17.** Sketch of the disk around MWC 349 seen edge on. Because of the small inclination angle, only emission from sector 1 where the radial velocity is small will reach the observer. Light from other places, for example, from the points marked 2, 3, and 4 is absorbed by the bulge.

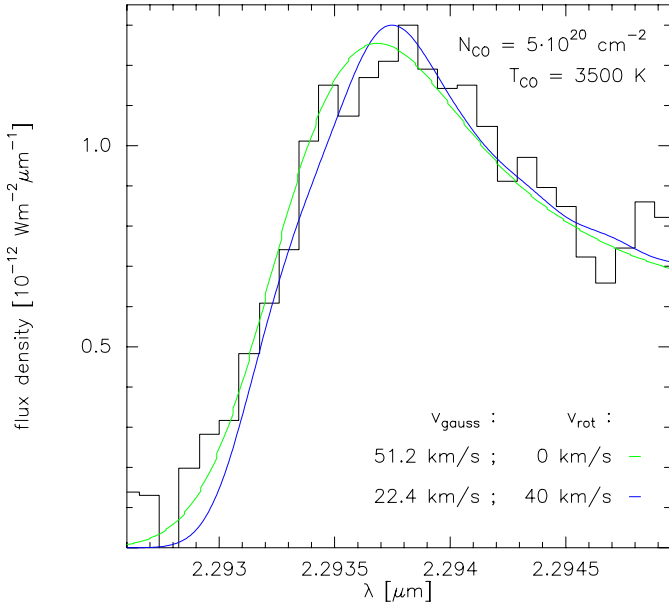


**Fig. 16.** Best fits to the observed 2 → 0 band head. The grey line represents the pure gaussian fit of Figure 13 and the black line shows the combination of a rotational component and a gaussian velocity component whose velocities are determined according to Eq. 11.

The scenario of a pure wind is very vague in its details, but gives a remarkably good fit. We might think of dense molecular blobs emanating from the disk. The total emission area of the blobs is  $\sim 0.6 \text{ AU}^2$ .

**Table 5.** Angles  $\theta$  and velocity ranges  $v_{\text{rot,los}}$  for the calculated sectors shown in Figure 18. The inclination angle was taken as  $10^\circ$  and the rotational velocity is  $98 \text{ km/s}$ .

	$\theta [^\circ]$	$v_{\text{rot,los}} [\text{km/s}]$
dashed line	180	-96.5 ... 96.5
solid line	75	-59.0 ... 59.0
dotted line	33	-27.6 ... 27.6

But there is still another alternative with  $N_{\text{CO}} \sim 5 \cdot 10^{20} \text{ cm}^{-2}$ , which we discuss now. If the CO band emission arises in the disk, it must come from inside the evaporation radius of the dust,  $r_{\text{evap}}$ , because of its high temperature of  $\sim 3500 \text{ K}$ . According to the Kraus et al. model of the dust disk, the distance is then smaller than  $2.88 \text{ AU}$  according to a rotational velocity greater than  $90 \text{ km/s}$ . Let us assume  $v_{\text{rot}} \simeq 100 \text{ km/s}$ . To avoid the problems with the line profile in case of such a high  $v_{\text{rot}}$ , as discussed in subsection 4.2 and demonstrated in Figure 14, we propose a configuration as depicted in Figure 17. The disk has a bulge and because of its small inclination angle  $i \sim 10^\circ$ , this bulge blocks the light from the inner

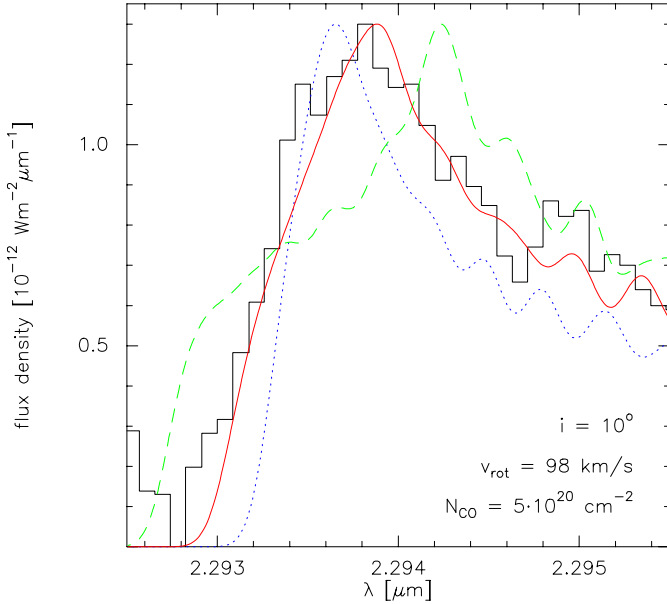


**Fig. 18.** Fit to the observed  $2 \rightarrow 0$  band head for ring segments with a Keplerian velocity of  $v_{\text{rot}} \simeq 100$  km/s. The geometry is depicted in Fig. 17. The angles and the corresponding velocity ranges are given in Table 5. The best fit is shown by the solid line.

edge of the disk on the near side to the observer. We therefore receive emission only from sector 1 in Figure 17 where the *radial* velocity is low. In Figure 18 we show computations of the flux received from sector 1 for different opening angles  $\theta$ . The ranges of radial velocities in the sectors are summarized in Table 5.

## 6. Conclusions

We present low and high resolution spectra in the near infrared of the B[e]-star MWC 349. The wavelength interval  $2.285$ – $2.342$   $\mu\text{m}$  contains mainly emission of the first overtone bands of the CO molecule as well as the Pfund series of atomic hydrogen. From modeling the Pfund lines under the assumption that they are optically thin, we find that they come from the inner part of the H II region around MWC 349 and are in LTE. The hydrogen line profiles are approximately gaussian and their width indicates a wind velocity of  $\sim 50$  km/s.

The CO molecules are at a temperature of  $3500$ – $4000$  K, the population of the vibrational levels is close to LTE. The width of the  $2 \rightarrow 0$  band head indicates a velocity broadening of the order of  $50$ – $60$  km/s, depending on the broadening mechanism, wind or rotation. The location of the hot CO gas producing the band emission could not be clarified, but we were able to propose several scenarios.

Because the CO as well as the Pfund lines can be fitted with a gaussian velocity component of  $\sim 50$  km/s, the first possibility is that the CO bands arise in the windy transition layer between the disk and the HII region, presumably in dense clumps

(see Fig. 13). The band head has in this case an optical depth of order unity ( $N_{\text{CO}} \simeq 5 \cdot 10^{20}$  cm $^{-2}$ ).

Alternatively, the CO might form in a thin layer above the dust disk at radii between  $6.5$  and  $15$  AU. In this scenario, the CO emission is optically very thin ( $N_{\text{CO}} \simeq 6 \cdot 10^{16}$  cm $^{-2}$ ;  $\tau \simeq 10^{-4}$ ), and the gas is thermally decoupled from the dust. As we could only produce fits of mediocre quality (see Fig. 15), due to the characteristic line profiles under Keplerian rotation (see Figure 14), this is not our favorite configuration.

Finally, we suggest that the CO bands come from the inner edge of the circumstellar disk. Because of the required high temperature and column density, the CO gas must be located inside the evaporation radius of the dust, i.e. at distances less than  $\sim 3$  AU from the star. Although this would imply a high rotational velocity component which would usually lead to a characteristic shoulder in the band profile, which is not observed, the disk may well have a bulge, as depicted in Figure 17. This bulge absorbs the CO emission from the near part of the rotating inner disk edge, so that the observer sees only a sector on the far side where the radial velocities are all smaller than  $\sim 60$  km/s. With such a geometrical configuration, a satisfactory fit is also possible (see Figure 18).

*Acknowledgements.* We would like to thank Frank Shu, the referee, for his helpful comments

## References

- Calvet, N., Patiño, A., Magris, C.G., D'Alessio, P., 1991, ApJ 380, 617
- Carr, J.S., 1989, ApJ 345, 522
- Carr, J.S., 1995, Ap & SS 224, 25
- Carr, J.S., Tokunaga, A.T., Najita, J., Shu, F.H., Glassgold, A.E., 1993, ApJ 411, L 37
- Chandler, C.J., Carlstrom, J.E., Scoville, N.Z., Dent, W.R., Geballe, T.R., 1993, ApJ 412, L 71
- Chandler, C.J., Carlstrom, J.E., Scoville, N.Z., 1995, ApJ 446, 793
- Chandra, S., Maheshwari, V.U., Sharma, A.K., 1996, A&AS 117, 557
- Cohen, M., Bieging, J.H., Dreher, J.W., Welch, W.J., 1985, ApJ 292, 249
- Dunham, J. L., 1932a, Phys.Rev. 41, 713
- Dunham, J. L., 1932b, Phys.Rev. 41, 721
- Farrenq, R., Guelachvili, G., Sauval, A. J., Grevesse, N., Farmer, C. B., 1991, J.Mol.Spectrosc. 149, 375
- Geballe, T.R., Persson, S.E., 1987, ApJ 312, 29
- Geisel, S.L., 1970, ApJ 161, L 105
- Green, T.P., Lada, C.J., 1996, ApJ 461, 345
- Hamann, F., Simon, M., 1986, ApJ 311, 909
- Hamann, F., Simon, M., 1988, ApJ 327, 876
- Hayashi, C., 1981, Suppl.Prog.Theor.Phys. 70, 35
- Kraus, M., 2000, PhD-Thesis, University of Bonn
- Kraus, M., Krügel, E., Hengel, C., Thum, C., 2000 *in preparation*
- Lamers, H.J.G.L.M., Zickgraf, F.-J., de Winter, D., Houziaux, L., Zorec, J., 1998, A&A 340, 117
- Leinert, C., 1986, A&A 155, L 6
- Mariotti, J.M., Chelli, A., Foy, R., Léna, P., Sibille, F., Tchounoutonov, G., 1983, A&A 120, 237
- Martin, S.C., 1997, ApJ 478, L 33
- Martín-Pintado, J., Bachiller, R., Thum, C., Walmsley, M., 1989, A&A 215, L 13

Menzel, D.H., Pekeris, C.L., 1935, MNRAS 96, 77  
Najita, J., Carr, J.S., Glassgold, A.E., Shu, F.H., Tokunaga, A.T., 1996,  
ApJ, 462, 919  
Rodríguez, L.F., Bastian, T.S., 1994, ApJ 428, 324  
Scoville, N., Hall, D.N.B., Kleinmann, S.G., Ridgeway, S.T., 1979,  
ApJ 232, L 121  
Smith, H.A., Strelnitski, V., Miles, J.W., Kelly, D.M., Lacy, J.H., 1997,  
AJ 114, 2658  
Storey, P.J., Hummer, D.G., 1995, MNRAS 272, 41  
Strelnitski, V.S., Haas, M.R., Smith, H.A., Erickson, E.F., Colgan,  
S.W.J., Hollenbach, D.J., 1996a, Sci 272, 1459  
Thum, C., Martín-Pintado, J., Bachiller, R., 1992, A&A 256, 507  
Thum, C., Martín-Pintado, J., Quirrenbach, A., Matthews, H.E., 1998,  
A&A 333, L 63  
Thum, C., Matthews, H.E., Martín-Pintado, J., Serabyn, E., Planesas,  
P., Bachiller, R., 1994b, A&A 283, 582  
Thum, C., Strelnitski, V.S., Martín-Pintado, J., Matthews, H.E., Smith,  
H.A., 1995, A&A 300, 843  
White, R.L., Becker, R.H., 1985, ApJ 297, 677